POLITECNICO DI TORINO
Repository ISTITUZIONALE

Wave focusing and related multiple dispersion transitions in plane Poiseuille flows

(Article begins on next page)

24 April 2024

F. Fraternale, G. Nastro and D. Tordella

View Online **Export Citation** **CrossMark**

ARTICLES YOU MAY BE INTERESTED IN
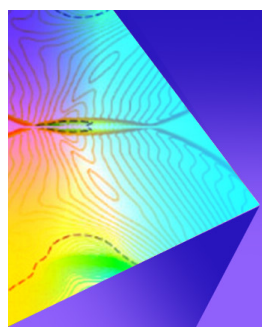
Physics of Fluids

Special Topic: Shock Waves

Submit Today!

AIP Publishing

Wave focusing and related multiple dispersion transitions in plane Poiseuille flows

View Online　　Export Citation　　CrossMark

F. Fraternale,[a] (iD) G. Nastro,[b] (iD) and D. Tordella[c] (iD)

AFFILIATIONS

Dipartimento di Scienza Applicata e Tecnologia, Politecnico di Torino, Torino 10129, Italy

[a]Present address: Center for Space Plasma and Aeronomic Research, The University of Alabama in Huntsville, Huntsville, Alabama 35805, USA.
[b]Present address: ISAE-SUPAERO, Université de Toulouse, Toulouse, France 31055.
[b]Author to whom correspondence should be addressed: daniela.tordella@polito.it

ABSTRACT

Motivated by the recent discovery of a dispersive-to-nondispersive transition for linear waves in shear flows, we accurately explored the wavenumber-Reynolds number parameter map of the plane Poiseuille flow in the limit of least-damped waves. We have discovered the existence of regions of the map where the dispersion and propagation features vary significantly from their surroundings. These regions are nested in the dispersive, low-wavenumber part of the map. This complex dispersion scenario demonstrates the existence of linear dispersive focusing in wave envelopes evolving out of an initial, spatially localized, three-dimensional perturbation. An asymptotic wave packet's representation, based on the saddle-point method, allows to enlighten the nature of the packet's morphology, in particular, the arrow-shaped structure and spatial spreading rates. A correlation is also highlighted between the regions of largest dispersive focusing and the regions which are most subject to strong nonlinear coupling in observations.

Published under license by AIP Publishing. https://doi.org/10.1063/5.0037825

I. INTRODUCTION

Dispersion is a fundamental property of traveling waves, and its terminology stems from types of solutions rather than types of governing equations, as well explained in the 1974 monography by Whitham[1] dedicated both to linear and nonlinear waves. It is commonplace to talk about dispersive equations: well-known examples of linear and nonlinear dispersive partial differential equations are the Airy, Euler–Bernoulli beam, Klein–Gordon, Schrödinger, Korteweg–de Vries, and Boussinesq equations. The reader can find general information in Refs. 2–4.

Dispersive wave focusing, i.e., the time-space localization of wave-train energy, is frequently encountered in physical sciences in very diversified areas. This mechanism relies on the phase modulation of perturbation wave-trains and produces regions in which disturbances can "focus" and reach finite amplitudes. Mention can be made of two examples: surface waves on water of finite depth, where dispersive focusing was suggested as a giant wave generation mechanism,[5–9] and wave-guides in integrated optical circuits.[10] In particular, in the field of water surface waves, the new knowledge of propagation pairing of long waves with short waves, and the interplay of their angle of inclination, introduces a new interpretation tool into the analysis of both

linear and nonlinear wave interactions. This dynamical aspect has not been considered in great detail in the study of turbulence transition. To date, dispersive focusing has not yet been reported in the field of perturbation waves traveling in nonstratified bounded flows within the framework of the Navier–Stokes equations.

In these flows, propagating waves are at the root of fluid flow instability and transition to turbulence. In particular, the growth of wave packets or localized spots is of great interest in the subcritical route to turbulence, also known as bypass transition.[11] In the past literature, the propagation and dispersion features of such internal waves have attracted less attention than the transient mechanisms responsible for their potential amplification, a process which was hitherto considered as the cause of transition to turbulence and, in the last few decades, has been framed within theories based on non-normal growth (see, e.g., Refs. 12 and 13).

In the past, many authors have devoted attention to such perturbation waves in shear flows, while no accurate characterization of their dispersion properties has been conducted so far. Linear and nonlinear wave dispersive focusing may be a potential agent of the catastrophic transition to turbulence observed for larger Reynolds numbers than the transitional thresholds beyond which uniform turbulence is observed, instead of the coexistence of laminar and turbulent patches.

In fact, the morphology of wave packets in shear flows has been mainly described through information concerning the global structure, deduced either from laboratory experiments[14–21] or from Navier–Stokes direct numerical simulations (DNSs),[22–24] where it is not easy to pick out the dynamics of the individual wave component.

The present study deals with a recently discovered instance of the complexity of dispersion properties for linear waves traveling within viscous, incompressible fluid flows governed by the Navier–Stokes equations under linearized dynamics. We intend to show that this uneven scenario in wave dispersion features allows to gather significant information about the morphology and propagation of localized, three-dimensional (3D) disturbances in bounded flows. In particular, the system we consider is the planar Poiseuille flow (PPF) between two infinitely long, parallel plates at a fixed distance $2h$ apart, as sketched in Fig. 1. This flow is driven by a pressure gradient in the flow direction and is retarded by viscous drag along both plates, so that these forces are balanced.

Previously, we demonstrated the existence of a sharp dispersive-to-nondispersive transition in PPF and wake flows for (normalized) wave number values near unity.[25–27] This was done by numerically computing the long-term dispersion relation of the Orr–Sommerfeld (OS) and Squire eigenvalue problem[28,29] within a four-decade range of the Reynolds number ($\mathcal{R}$) and a three-decade range of wavenumbers (k). Here, a detailed computation has been carried out for the phase velocity and the local group velocity of least-damped OS modes, extending the previous analyses in the limit of small wavenumbers. We adopt the generalization of the concept of the group velocity given by Whitham[1] for wave packets in purely dispersive homogeneous media to the case of dispersive and dissipative media.[30–32]

We will first present newly discovered properties of wave dispersion in PPF. These features appear as transitions of the dispersion nature of the least-damped OS mode in the $\mathcal{R} - k$ map (hereinafter also referred to as dispersion map). In particular, we show the existence of several regions in the small-wavenumber portion of this map where wave dispersion characteristics change significantly from the surroundings, and the nature of the least-damped OS mode changes as well.
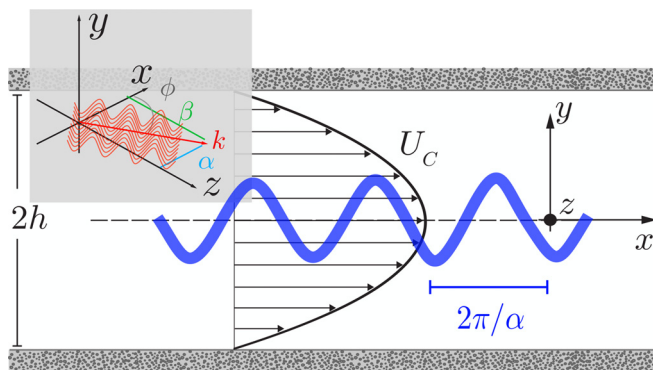
FIG. 1. Sketch of the plane Poiseuille flow, coordinate system, and 3D wave perturbation. The reference velocity is the centerline velocity U_C, and the reference length is the half thickness of the channel, h. The Reynolds number is then $\mathcal{R} = hU_C/\nu$, where ν is the kinematic viscosity of the fluid. The planar wavenumber vector and the wave angle of the perturbation are respectively $\boldsymbol{k} = \alpha\boldsymbol{e_x} + \beta\boldsymbol{e_z}$ and $\phi = \tan^{-1}(\beta/\alpha)$.

Then, we show that this picture produces linear dispersive focusing. In fact, when a wave packet is assembled via superposition of monochromatic waves ranging from the smallest to the largest wavenumber considered here, both the following occur, that is, components having similar wavenumbers can propagate with different speeds, which yields dispersion, and, on the other hand, waves with distinct wavelength can show very similar propagation features. Via a simple propagation scheme,[33] we highlight the existence of multiple loci for dispersive focusing in the physical space where the packet propagates. Since dispersive effects are known to play a leading role in pattern formation and wave dynamics (see, e.g., Ref. 34), this new propagation scenario can help to understand the morphology of perturbation clusters and wave packets, at least in their early evolution before nonlinear effects occur, triggering secondary flow bifurcations that are not predicted by the linear approach. In fact, we show that the described focusing explains the major features of the morphology and propagation of localized, 3D disturbances (or spots) in channel flows, such as the arrow-shaped structure, the leading streaks, and the trailing waves at the spot's wingtips. The comparison of our results with laboratory experiments also suggests that wave focusing in the early linear phase may play an important role in the onset of nonlinear coupling and consequent transition to turbulence in shear flows. This topic will need to be further investigated in a future study.

The paper is organized as follows. In Sec. II, we recall the physical problem and the mathematical model. The results concerning the dispersion relation of PPF are discussed in Sec. III. The unsteady evolution of localized wave packets and their asymptotic representation are presented in Sec. IV, and conclusions are drawn in Sec. V. Appendix is devoted to the technical details about our numerical simulations.

II. PHYSICAL PROBLEM AND MATHEMATICAL FRAMEWORK

We consider the plane Poiseuille flow (PPF), where inertia and molecular diffusion are the two only players. Figure 1 presents a longitudinal cut of the channel and reports the coordinate system and the reference quantities used for normalization. We consider as characteristic length and velocity scales the half height of the channel h and the centerline velocity U_C, respectively. As we address incompressible buoyancy-free flows, the governing equations are the Navier–Stokes equations which read in dimensionless form

$$\boldsymbol{\nabla} \cdot \boldsymbol{u} = 0, \tag{1}$$

$$D_t\boldsymbol{u} = -\boldsymbol{\nabla}p + \frac{1}{\mathcal{R}}\Delta\boldsymbol{u}, \tag{2}$$

where $D_t = \partial_t + (\boldsymbol{u} \cdot \boldsymbol{\nabla})$ denotes the material derivative and $\mathcal{R} = hU_C/\nu$ is the Reynolds number with ν the fluid kinematic viscosity. No-slip boundary conditions are imposed at the walls ($\boldsymbol{u} = 0$ at $y = \pm1$). The parallel basic flow $\boldsymbol{U} = U(y)\boldsymbol{e_x}$ consists of the well-known parabolic profile of Poiseuille, stationary solution of Eqs. (1) and (2),

$$U(y) = 1 - y^2. \tag{3}$$

The governing equations for a small perturbation, $\tilde{\boldsymbol{u}} = \boldsymbol{u} - \boldsymbol{U}$, $\tilde{p} = p - P$, are obtained by linearizing Eqs. (1) and (2) about the basic flow (3),

$$\boldsymbol{\nabla} \cdot \tilde{\boldsymbol{u}} = 0, \tag{4}$$

$$\partial_t \tilde{\boldsymbol{u}} + \boldsymbol{U} \cdot \nabla \tilde{\boldsymbol{u}} + \tilde{\boldsymbol{u}} \cdot \nabla \boldsymbol{U} = -\nabla \tilde{p} + \frac{1}{\mathcal{R}} \Delta \tilde{\boldsymbol{u}}. \tag{5}$$

We resort to both a modal and nonmodal approach in order to determine linear wave disturbances that are likely to grow over the Poiseuille's profile. Taking into account the streamwise and spanwise homogeneity of the base flow (3), a general perturbation $\tilde{\boldsymbol{q}} = [\tilde{\boldsymbol{u}}, \tilde{p}] = [\tilde{u}, \tilde{v}, \tilde{w}, \tilde{p}]$ can be expressed as a Fourier integral,

$$\tilde{\boldsymbol{q}}(\boldsymbol{x}, t) = \int_{-\infty}^{+\infty} \hat{\boldsymbol{q}}(\boldsymbol{k}; y, t) e^{i\boldsymbol{k}\cdot\boldsymbol{x}} d\boldsymbol{k}, \tag{6}$$

where $\boldsymbol{k} = \alpha \boldsymbol{e_x} + \beta \boldsymbol{e_z}$ is the planar wavenumber vector of streamwise and spanwise components, α and β, respectively. The wave angle is defined as $\phi = \tan^{-1}(\beta/\alpha)$ (see Fig. 1).

We denote k the magnitude of the planar wavenumber vector and this convention will be used throughout the paper. By using the wall-normal velocity–vorticity formulation,[35] the linearized nonmodal equations in the wavenumber space read:

$$\left[(\partial_t + i\alpha U)(\partial_y^2 - k^2) - i\alpha U'' - \frac{1}{\mathcal{R}} (\partial_y^2 - k^2)^2 \right] \hat{v} = 0, \tag{7}$$

$$\left[(\partial_t + i\alpha U) - \frac{1}{\mathcal{R}} (\partial_y^2 - k^2) \right] \hat{\omega}_y = -i\beta U' \hat{v}, \tag{8}$$

where $\tilde{v}$ and $\tilde{\omega}_y$ are, respectively, the wall normal velocity and vorticity and the prime symbol stands for a derivation with respect to the wall-normal direction, y. The streamwise and spanwise velocity components can be easily recovered *a posteriori* from $\hat{v}$ and $\hat{\omega}_y$. The following expressions are obtained from the continuity equation (4) and from the definition of the velocity curl:

$$\hat{u} = \frac{i}{k^2} \left(\alpha \partial_y \hat{v} - \beta \hat{\omega}_y \right), \tag{9}$$

$$\hat{w} = \frac{i}{k^2} \left(\beta \partial_y \hat{v} + \alpha \hat{\omega}_y \right). \tag{10}$$

The boundary conditions associated with the linearized system [Eqs. (7) and (8)] are homogeneous and correspond to the no-slip condition:

$$\hat{v}(\pm 1) = \partial_y \hat{v}(\pm 1) = \hat{\omega}_y(\pm 1) = 0. \tag{11}$$

These boundary conditions are exactly satisfied by the Chandrasekhar–Reid functions used by our numerical method. Note that different basic flow profiles, such as boundary layers, wakes, or jets, may accept different boundary conditions (e.g., the exponential decay can be imposed at $|y| \to \infty$). The Fourier representation of Eq. (6) implies periodic boundary conditions at the x and z axes. In our numerical simulations described below, the domain is large enough to prevent boundary effects on the solution.

III. LONG-TERM ASYMPTOTICS OF SMALL-AMPLITUDE WAVES

A. Modal analysis approach

The long-term asymptotic limit ($t \to \infty$) is obtained by imposing to Eqs. (7) and (8) the harmonic structure for the perturbations, i.e., $\partial_t \to -i\sigma$, where $\sigma(\boldsymbol{k}; \mathcal{R}) = \sigma_r(\boldsymbol{k}; \mathcal{R}) + i\sigma_i(\boldsymbol{k}; \mathcal{R})$ is a complex OS eigenvalue, defining the dispersion relation for the corresponding

eigenmode. Let us recall that for bounded flows, the OS spectrum has infinitely many discrete eigenvalues. The dispersion relation $\sigma(\boldsymbol{k}; \mathcal{R}) \equiv \omega(\boldsymbol{k}; \mathcal{R}) = \omega_r + i\omega_i$ is computed by solving numerically the eigenvalue problem associated with Eqs. (7) and (8). We adopt a fifth-order accurate Galërkin method based on Chandrasekhar–Reid functions,[36] described in detail in Refs. 25 and 27. The modal analysis approach yields the complex angular frequency whose real part ω_r allows to define the phase velocity

$$\boldsymbol{c} \equiv \frac{\omega_r}{k} \boldsymbol{e}_k, \tag{12}$$

where $\boldsymbol{e}_k = \cos(\phi)\boldsymbol{e}_x + \sin(\phi)\boldsymbol{e}_z$ stands for the direction cosine of planar wavenumber vector $\boldsymbol{k}$. The real group velocity is computed via numerical derivative from the kinematic definition

$$\boldsymbol{v}_{\mathrm{g}} \equiv \nabla_k \omega_r, \tag{13}$$

where $(\nabla_k)_i \equiv \partial/\partial k_i$ is the gradient in the wavenumber space. The corresponding imaginary part $\nabla_k \omega_i$ was also computed, and the discussion on its role will be resumed later in Sec. IV. A dispersion factor, $\boldsymbol{f}_d$, can be defined as the difference between the group and the phase speeds

$$\boldsymbol{f}_d(\boldsymbol{k}) \equiv \boldsymbol{v}_{\mathrm{g}}(\boldsymbol{k}) - \boldsymbol{c}(\boldsymbol{k}). \tag{14}$$

In general, for a linear dispersion relation, the group velocity $\boldsymbol{v}_{\mathrm{g}}$ coincides with the phase velocity $\boldsymbol{c}$ and a wave envelope with the central wavenumber $\boldsymbol{k}$ is said to be nondispersive. In this case, $\boldsymbol{f}_d = \boldsymbol{0}$. For quadratic dispersion relations instead, $\boldsymbol{f}_d(\boldsymbol{k})$ represents exactly the directional spreading rate of the wave envelope. In the general case of higher order nonlinear dispersion relations, the wave packet undergoes both a spatial spreading and a distortion, and $|\boldsymbol{f}_d|$ is an increasing function of these processes. In the following, the sign of $\boldsymbol{f}_d$ will be kept in order to retain information about whether the packet travels faster ($\boldsymbol{f}_d > \boldsymbol{0}$) or slower ($\boldsymbol{f}_d < \boldsymbol{0}$) with respect to the central wavenumber.
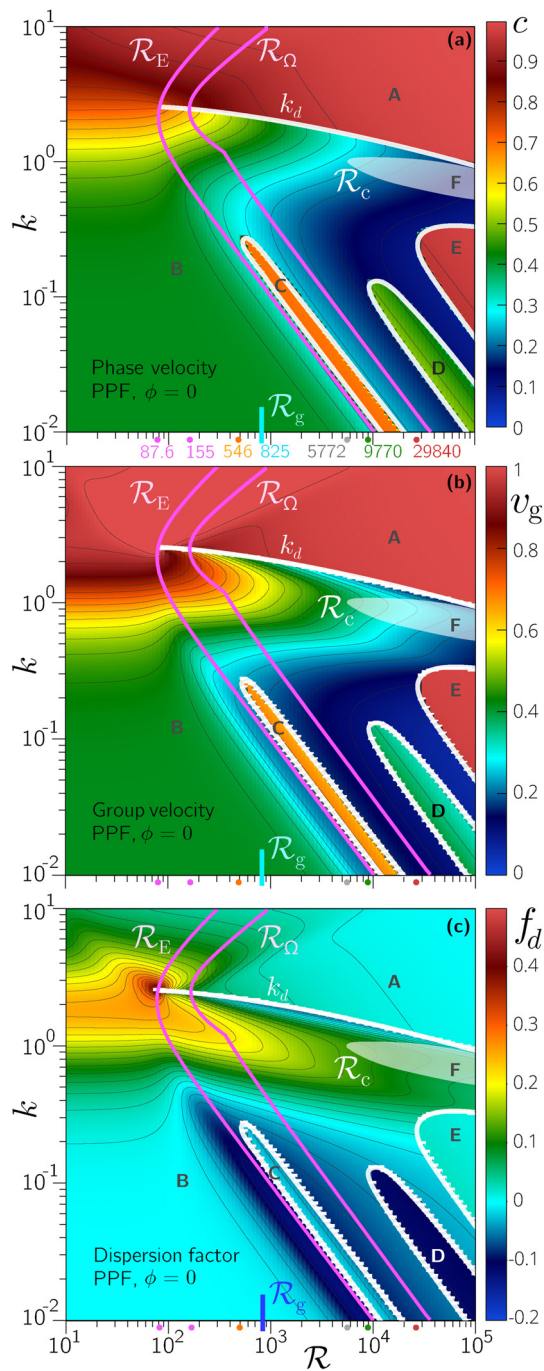
B. Dispersion maps

We focus on the dispersion relation of least-damped OS mode, i.e., the mode that experiences the largest exponential growth. These results will be used in Sec. IV to model the asymptotic dynamics of wave packets in the PPF. Results are presented in Fig. 2. The three panels in Fig. 2 show the magnitude of the phase velocity c (a), the group velocity v_g (b), and the dispersion factor f_d (c), respectively, for longitudinal waves ($\phi = 0$) seen in their long-term evolution. In the maps shown in Fig. 2, the longitudinal wavenumber ($k \equiv \alpha$) and the Reynolds number are uniformly distributed in the log-space, over a grid of 100×240 points, respectively, with $\mathcal{R} \in [10, 10^5]$ and $k \in [10^{-2}, 10]$.

The existence of several sub-regions is highlighted in Fig. 2 (labeled with letters **A** to **F**). The net separation between such regions is due to the change of identity of the leading OS mode. Note that the boundary of each sub-region has been enhanced for the clarity of visualization. In panel (a), the smallest Reynolds number for which a sub-region is found is also reported.

A first observation is the sharp separation between the fast non-dispersive waves of sub-region **A** ($c \approx v_{\mathrm{g}} \approx 1$ for $k > k_d$) and the slow dispersive waves of sub-region **B** ($k < k_d$), which ends up near

FIG. 2. Dispersion relation of the least-damped mode of longitudinal waves in PPF, $\mathcal{R} \in [10, 10^5]$ and $k \in [10^{-2}, 10]$. The maps contain 100×240 $(\mathcal{R}, k)$ simulations, uniformly distributed in the log–log space. (a) Phase velocity, *c*. (b) Group velocity, v_g. (c) Dispersion factor, $f_d = v_g - c$. k_d is a dispersion threshold[25] that bounds the nondispersive sub-region **A**. The pink curves, $\mathcal{R}_E(k), \mathcal{R}_\Omega(k)$, represent the lower bounds for kinetic energy and enstrophy transient growth, respectively.[26] In the low-k part of the maps, three sub-regions **C**, **D**, **E**, have different dispersion properties than the surroundings (**B**). Sub-region **F** represents the asymptotic instability region.

the nose at $\mathcal{R}_E(k) \approx 87.6$ and $\alpha \approx 2.5$. We name the threshold wavenumber $k_d(\mathcal{R})$ (white curve). As mentioned in Sec. I, the existence of sub-region **A** was first shown in our previous studies.[25,26] Interestingly, the map in the neighborhood of $\mathcal{R} \approx 87.6$ and $\alpha = 2.5$ is characterized by a high level of dispersion, as can be deduced from f_d in panel (c). The upper boundaries of the two-dimensional monotonic stability regions for the kinetic energy and the enstrophy of perturbation waves are reported in Fig. 2 with the pink curves $\mathcal{R}_E(k)$ and $\mathcal{R}_\Omega(k)$, respectively. The meaning of these thresholds is that transient growths of energy/enstrophy are only possible for larger $\mathcal{R}$ than the respective limit value, whatever initial condition is specified in the initial-value problem.[13,37] The analytical derivation of the enstrophy curve can be found in the work of Fraternale *et al.*[26] The white shadowed region in Fig. 2 denotes the well-known unconditional instability region, **F**. Here, the dominant OS eigenvalue is characterized by $\sigma_i > 0$. This region is located in the dispersive part of the graph, just below the curve $k_d(\mathcal{R})$, for $\mathcal{R} > 5772.22.$[38]

A remarkable finding is the existence of the three sub-regions **C**, **D**, and **E**, which have different dispersion features from their surroundings and are located in the dispersive, lower part of the map at $\mathcal{R} > 576$. These regions appear tilted at 45° in the log–log plane. It should be noted that the $f = f[\log(k\mathcal{R})]$ trend is recurrent for low wavenumbers in all types of stability maps, not only as regards the monotonic boundaries mentioned previously and the asymptotic phase velocity, but also pertaining to the maximal transient growth of kinetic energy and enstrophy (see also Fig. 8 in Appendix). Thus, looking at the map from small to large wavenumbers under fixed flow conditions, that is at constant $\mathcal{R}$, least-damped modes can be observed across a number of fluctuations of the dispersion and propagation properties. As a consequence, waves with distant wavelengths can have the same group speed value, producing a linear dispersive focusing, which may significantly change as $\mathcal{R}$ varies.

In detail, sub-region **C** is found at $\mathcal{R} > 545$ and $k < 0.28$. It contains anti-symmetric wall-modes (A-family, but close to S-family modes, according to the classification made by Mack[39]) having intermediate phase speed $c \approx 0.7$, pretty much equal to the group velocity v_g. Then, the dispersion level in **C** is low and lower than that of the surrounding part of the map. Sub-region **D** is met at $\mathcal{R} > 9770$ and $k < 0.13$; thus, it lies below the unconditional instability region **F**. Here, the identity of the eigenmodes is the same as in sub-region **C**. However, these solutions travel with a smaller phase speed, $c \approx 0.45$, which slightly depends on the wavenumber k, leading to high dispersion for wave packets containing this range of wavenumbers. In particular, the group speed ($v_g \approx 0.35$) is higher compared to the background region [see Fig. 2(b)] and smaller than the phase speed c [see panel (c)]. The third sub-region (**E**) is met at $\mathcal{R} > 29\,840$ and $k < 0.35$. In this case, the least-damped mode belongs to the right branch of the spectrum (P-family); it is an anti-symmetric, fast ($c \approx 1$), and central mode. Therefore, the behavior in this region is quite the same as in the nondispersive part of the map at $k > k_d$ (sub-region **A**). A common feature to all the three sub-regions is that they are the only parts of the map where the leading mode (stable, in all cases) is anti-symmetric. In the case of oblique waves ($\phi \neq 0$), we recall that the dispersion relation of the least-damped mode can be deduced from the longitudinal case described in Fig. 2 via the Squire's transformation[29]

$$\omega_{3D}(k, \mathcal{R}) = \omega_{2D}(k, \alpha/k\mathcal{R}). \tag{15}$$

Thus, with increasing ϕ, the map structure remains unchanged, apart from a shift toward higher $\mathcal{R}$, in the log–log plot (this of course does not apply to the curves $\mathcal{R}_E$, $\mathcal{R}_\Omega$). Concurrently, both the phase velocity and the group velocity decrease by a factor equal to $\cos(\phi)$, and eventually the phase speed of an oblique wave with wavenumber $\boldsymbol{k}$ reads

$$\boldsymbol{c}_{3D}(\boldsymbol{k}; \mathcal{R}) = \boldsymbol{c}_{2D}(|\boldsymbol{k}|; \mathcal{R}\cos\phi)\cos\phi. \tag{16}$$

IV. WAVE PACKET ASYMPTOTIC REPRESENTATION

The dispersion relation $\omega(\boldsymbol{k}; \mathcal{R})$ described in Sec. III can be used to obtain an approximate asymptotic representation of a local impulsive disturbance. A wave packet can be formally represented by means of the following Fourier integral:

$$\tilde{q}(\boldsymbol{x}, t) = \int_{-\infty}^{+\infty} \hat{q}(\boldsymbol{k}) e^{i\theta(\boldsymbol{k};\boldsymbol{x},t)} d\boldsymbol{k}, \tag{17}$$

where $\tilde{q}$ is any relevant physical quantity and $\theta(\boldsymbol{k};\boldsymbol{x},t) \equiv \boldsymbol{k} \cdot \boldsymbol{x} - \omega(\boldsymbol{k})t$ represents the phase. Let us consider the Taylor series expansion of the dispersion relation around an arbitrary wavenumber $\boldsymbol{k}_0$,

$$\omega(\boldsymbol{k}) = \omega(\boldsymbol{k}_0) + \nabla_k\omega|_{\boldsymbol{k}_0} \cdot (\boldsymbol{k} - \boldsymbol{k}_0)$$
$$+ (\boldsymbol{k} - \boldsymbol{k}_0)^T \boldsymbol{H}_\omega|_{\boldsymbol{k}_0}(\boldsymbol{k} - \boldsymbol{k}_0) + \mathcal{O}(||\boldsymbol{k} - \boldsymbol{k}_0||^3), \tag{18}$$

where $(\boldsymbol{H}_\omega)_{ij} \equiv \frac{\partial^2 \omega}{\partial k_i \partial k_j}$ is the Hessian matrix. By truncating the series at the linear term, Eq. (17) becomes

$$\tilde{q}(\boldsymbol{x}, t) \approx e^{i\boldsymbol{k}_0 \cdot \boldsymbol{x} - i\omega(\boldsymbol{k}_0)t} \int_{-\infty}^{+\infty} \hat{q}(\boldsymbol{k}) e^{i(\boldsymbol{k} - \boldsymbol{k}_0) \cdot (\boldsymbol{x} - \nabla_k\omega|_{\boldsymbol{k}_0}t)} d\boldsymbol{k}, \tag{19}$$

where the first factor indicates a monochromatic wave developing in time, according to $\exp[\omega_i(\boldsymbol{k}_0)t]$, and moving with a phase speed $\boldsymbol{c}_0 = \omega_r(\boldsymbol{k}_0)/||\boldsymbol{k}_0|| \, \boldsymbol{e}_k$, while the second factor represents the wave packet envelope near $\boldsymbol{k}_0$ that travels with the group speed $\boldsymbol{v}_g = \nabla_k\omega_r|_{\boldsymbol{k}_0}$ and dissipates energy in the fluid medium depending on $\nabla_k\omega_i|_{\boldsymbol{k}_0}$, as recently discussed by Gerasik and Stastna.[32] Since the viscosity plays a dual role in our system, being the cause of both the flow instability and the damping, it would be interesting to extend to our context the analysis of Ref. 32, including both the dissipation outflux and the molecular diffusive process in the interpretation of the complex group speed. The interpretation by Muschietti and Dum,[30] where $\nabla_k\omega_i$ is related to the differential damping among the Fourier components and thus to the slow drift of the central wave number along the packet trajectory, is also very important in our view and can be considered complementary to that of Ref. 32. Equation (19) helps to understand the concept of energy-carrier wave and the role of the group velocity, but it is no longer useful to describe the dispersion phenomenology which can lead to a distortion of the initial envelope shape. Looking for the asymptotic form (large t with $\boldsymbol{x}/t$ of order unity), the steepest-descent method (also referred to as the saddle-point method)[40,41] leads to the following expression:

$$\tilde{q}(\boldsymbol{x}, t) \approx \hat{q}(\boldsymbol{\kappa}) \left(\frac{2\pi}{t}\right)^{\frac{n}{2}} \sqrt{\frac{1}{|\det(\boldsymbol{H}_\omega(\boldsymbol{\kappa}))|}}$$
$$\times e^{i\left\{\boldsymbol{\kappa} \cdot \boldsymbol{x} - \omega(\boldsymbol{\kappa})t - \frac{\pi}{4}\text{sign}[\det(\boldsymbol{H}_\omega)]\right\}}$$
$$= A(\boldsymbol{x}, t)e^{i\chi(\boldsymbol{x},t)}, \tag{20}$$

where n is the space dimension ($n = 2$ in the case of planar waves) and $\boldsymbol{\kappa}$ is the specific wavenumber which makes the phase θ of the integral (17) stationary

$$\boldsymbol{\kappa} : \nabla_k\theta(\boldsymbol{\kappa}) \equiv \boldsymbol{x} - \nabla_k\omega(\boldsymbol{\kappa})t = \boldsymbol{0}, \tag{21}$$

$$\Rightarrow \begin{cases} \boldsymbol{x}/t = \nabla_k\omega_r(\boldsymbol{\kappa}) \equiv \boldsymbol{v}_g \\ 0 = \nabla_k\omega_i(\boldsymbol{\kappa}). \end{cases} \tag{22}$$

The $\frac{1}{2}$ exponent at the second and third factors in Eq. (20) is related to the first nonzero term in the expansion (18), which here is assumed to be the term including second derivatives. If Eq. (21) has solutions $\boldsymbol{\kappa}(\boldsymbol{x}, t)$, this means that a specific wavenumber, $\boldsymbol{\kappa}$, dominates the packet in the physical space defined by Eq. (22). In particular, the disturbance is a space- and time-dependent wave packet, whose local frequency is $\omega_r(\boldsymbol{\kappa})$ at the space location $\boldsymbol{x}$ and time instant t. In the general case of complex-valued dispersion relation, the disturbance experiences a transient growth or damping, which is given by the factor $\exp[\omega_i(\boldsymbol{\kappa})t]$, in addition to the amplitude factor $A(\boldsymbol{x}, t)$ of Eq. (20). Note that early applications of this method to the field of hydrodynamics for shear flows are found, e.g., in Refs. 33 and 42–44. Indeed, for homogeneous media, the theory of wave groups with slowly varying properties leads to the conservation of wavenumbers and wave angles along straight lines in the $\boldsymbol{x} - t$ plane. Differently than in the previous studies, we will not use analytic models of the dispersion relation. Instead, we use the exact results shown in Sec. III, as described below.

Results from the implementation of the saddle-point method in PPF are shown in Figs. 3, 4(a), and 4(b) (Multimedia view) for $\mathcal{R} = 1000$ and in Fig. 6 for $\mathcal{R} = 500, 1000, 2000,$ and 4000. As shown in Sec. III, the group velocity of the least-damped wall-normal velocity mode is computed from the exact dispersion relation of 3D waves. These figures show the long-term space distribution, in the x–z plane, of a wave packet initially localized at the origin ($x = z = 0$). The coordinates of Figs. 4 and 6 are normalized over time, so that they represent the group velocity. Therefore, the spreading rates can be directly inferred from the figures. For each $\mathcal{R}$, the wave packet is made of a discrete number of vector wavenumbers, $N_w = 57\,600$. In particular, we set a uniform grid for both the streamwise and the spanwise wavenumber components, $\alpha \in [10^{-2}, 10]$, $\beta \in [-5, 5]$, and the grid spacing is $\Delta\alpha = \Delta\beta = 0.0417$. For each vector wavenumber, the least stable OS mode is computed and then propagated according to Eq. (22). Therefore, each point in our figures represents an individual wave component. The corresponding wavenumber and wave angle are color-coded.

Figure 3 shows the imaginary part of the group velocity. Due to the limited differential damping among the OS leading modes, the normalized components of the imaginary part of the group velocity are small. For instance, at $\mathcal{R} = 1000$, the x-component is in the range $(-0.03, 0.08)$ for about 95% of the wavenumbers considered in this study, while the z-component is within $(-0.03, 0.03)$ (see Fig. 3).
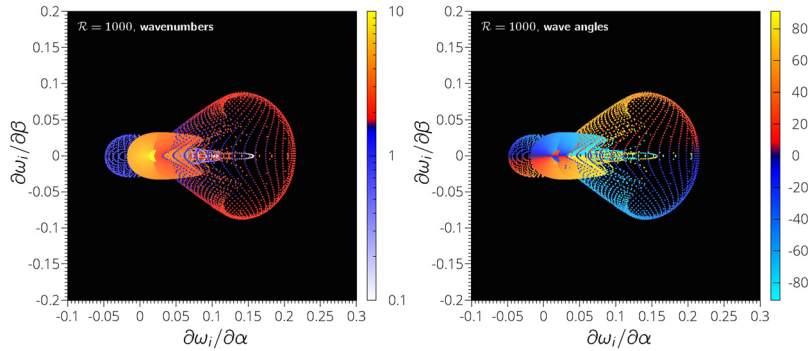
FIG. 3. Gradient of the imaginary part of the dispersion relation for the least damped OS mode for PPF at $\mathcal{R} = 1000$. Visualization in terms of wavenumber (left panel) and wave angle (right panel).

Therefore, since $\mathbf{\nabla}_k \omega_r(\mathbf{\kappa})/\mathbf{\nabla}_k \omega_i(\mathbf{\kappa}) \ll 1$, the second condition in Eq. (22) is found to be approximately satisfied by most of wavenumbers.

Figure 4 shows the asymptotic shape of the wave packet and compares it to both a numerical simulation of the linearized initial value problem and to a laboratory experiment. Specifically, panel (a) in Fig. 4 shows the results from Eq. (22) in terms of the wavenumber magnitude, while panel (b) displays the wave angle. The unsteady linear evolution of a 3D localized wave packet in PPF is investigated by integrating the linearized Navier–Stokes equations [Eqs. (7) and (8)] via our semi-analytic code based of Fourier and Chandrasekhar functions (see Appendix for further details). We should mention that for an extension of our analysis to weakly nonparallel flows, alternate stability analysis methods should be considered, such as the Parabolized Stability Equations (PSE) or the Wentzel–Kramers–Brillouin–Jeffreys (WBKJ), or (bi- and tri-)global stability methods in general (e.g., see Refs. 45–47).

Results of our numerical simulation at $\mathcal{R} = 1000$ are shown in panel (c). Here, we choose as initial condition a localized (at $x = z = 0$) wall-normal velocity disturbance with a Gaussian distribution in the x–z plane. The initial distribution along the y axis is such to guarantee a large energy growth rate. Technical details concerning simulation parameters are reported in Appendix. In panel (d), we reproduce Fig. 5 of the well-known laboratory experiment carried out by Carlson *et al.*[15] in 1982, showing a developed spot where turbulence and waves coexist. Note that this visualization has been accurately scaled in order to allow comparison with our simulation. To achieve this, information from Fig. 11 in Ref. 15 has also been used. In terms of normalized time, the experiment visualization is at $t = 180$. The choice of $t = 120$ for the simulation of panel (c) is essentially related to the fact that it is an intermediate state (intermediate asymptotics, see 1996 Barenblatt monography[48]) between the early transient—the short period when the morphology changes very rapidly—and the long term, when the linear packet has decayed. This time may depend on the flow parameters and initial conditions. At $t = 120$, the packet's propagation properties are nearly asymptotic, as shown in panels (a) and (d) of Fig. 9, which allows the comparison with the asymptotic representation. Note also that the maximal energy and enstrophy gain is reached at $t \approx 20$ ($t_{\text{dim}} \approx 0.2$ s), as shown in panels (e) and (f), of Fig. 9, so that the linear solution decays at large times. The comparison with experiments is meaningful only in the early/intermediate stage of these structures. Although in the experiment the spot at $t \approx 120$ has

already developed the turbulent core, it is interesting to look at the laminar wave regions surrounding the core. A first observation is that most of the typical features of the 3D wave packet are recovered by the representation of panels (a) and (b): the arrow pattern of the spot is made up of a slower almond-shaped rear part, a faster front, and a streaky tongue connecting these two regions. We highlight that a remarkable quantitative agreement is achieved between dominant wavenumbers and wave angles obtained from the asymptotic representation and those observed in the laminar wave patches of real spots. Typical vector wavenumbers for both the simulation and the laboratory experiment are reported in panels (c) and (d) of Fig. 4. The bulb-shaped front is difficult to observe in a laboratory because its wave components are highly damped. However, the nature of these nondispersive modes makes them relevant from the enstrophy viewpoint, as we have recently shown[26] (see also Ref. 49 in the context of pipe flows). The core of the wave packet can be recognized as the rhomboid-shaped region at $0.35 \lesssim x/t \lesssim 0.5$. Note that in panel (a) the color bar is set so that the nondispersive components $k > k_d \approx 2$ and the inner rhomboid part are highlighted. This pattern is typical of both the early- and the self-sustained evolution of the spot's life (see, for instance, Fig. 4 in Refs. 18 and 19, and Fig. 15 in Ref. 20).

Wave focusing can be measured by evaluating the concentration of wave components at specific locations in the x–z plane of the physical space. In practice, we discretize the x–z plane in 64×32 bins and compute the normalized histogram

$$\rho_w(x_j, z_j) \equiv \frac{n(x_j, z_j)}{N_w}, \qquad (23)$$

where $n(x_j, z_j)$ represents the number of waves in the jth bin, centered at (x_j, z_j), and $N_w = 57\,600$ denotes the total number of waves used in the asymptotic representation. Therefore, ρ_w represents the probability of finding—at a specific spatial location and in the long term—a wave component from the initial packet. Results are shown in Fig. 5 for the same parameters used in Fig. 4(c). It should be reminded that ρ_w is derived from the asymptotic model in the modal-stability framework. Therefore, it represents the probability of finding—at a specific space location—a wave component from the initial packet in the long-term limit. As discussed previously, it approximately represents the wave distribution in the intermediate transient. In the very short early stage, its distribution can be different and rapidly changing from the initial state where all waves are focused in the origin. It would be interesting
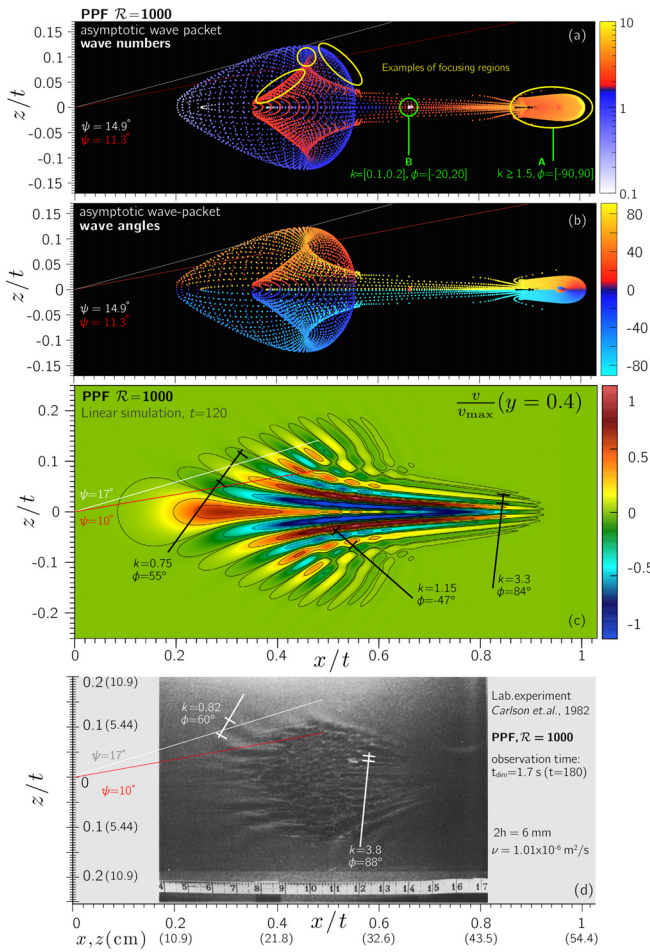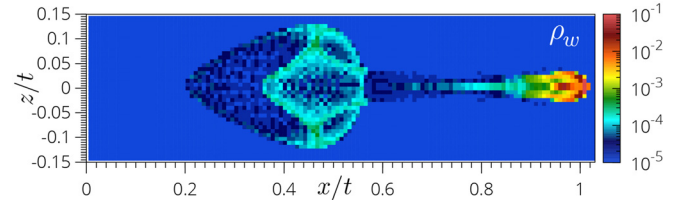
FIG. 4. Wave packet long-term propagation scheme, numerical simulation, and laboratory visualization at $\mathcal{R} = 1000$. (a) Wavenumber propagation. The regions of most intense wave focusing are highlighted with yellow and green circles. (b) Wave angle propagation. (c) Numerical simulation of the linearized initial-value problem [Eqs. (7) and (8), see also Appendix] for an initial Gaussian disturbance. Two visualization movies are available (Multimedia view). (d) Laboratory visualization adapted from Fig. 5 of D. R. Carlson, S. E. Widnall, and M. F. Peeters, "A flow-visualization study of transition in plane Poiseuille flow," J. Fluid Mech. **121**, 487–505 (1982). Copyright 1982 Cambridge University Press. Here, the axes have been normalized with $t_{\mathrm{dim}} = 1.7$ s derived from information in Fig. 11 of the same study and rescaled to match the other panels.

FIG. 5. Wave focusing, shown via the normalized histogram of wave components, see Eq. (23), for the wave packet asymptotic representation of Figs. 4(a) and 4(b), $\mathcal{R} = 1000$.
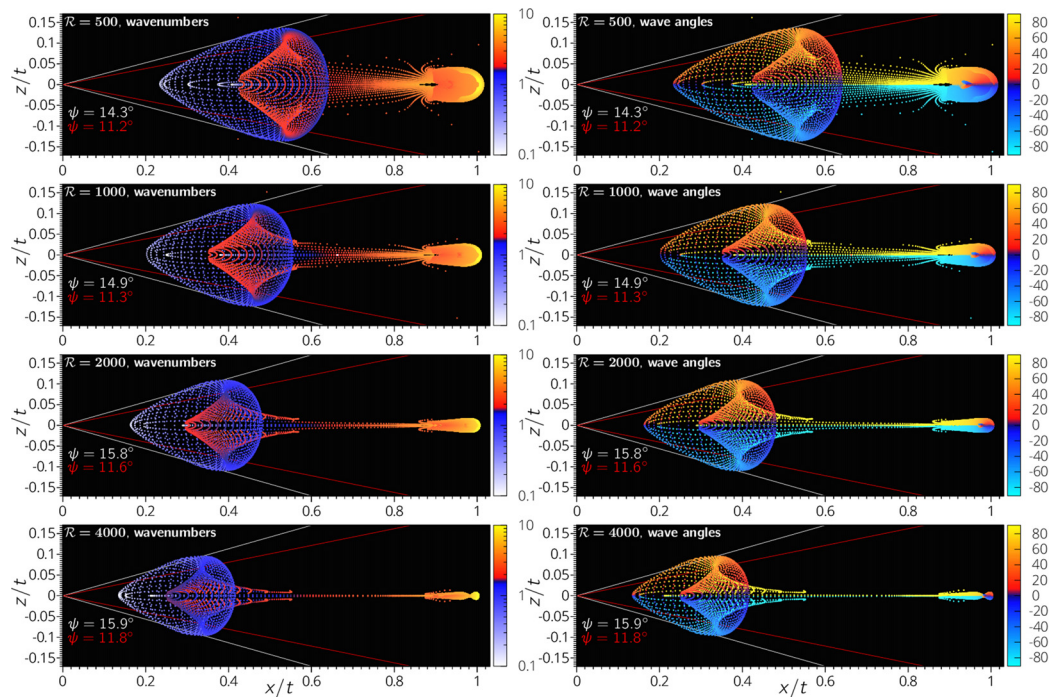
wave focusing is significant at the wingtips. This is consistent with the experimental observation that the transition to turbulence is first triggered at the wingtips.[15] Waves at the spot's leading edge are more oblique, nearly orthogonal to the basic flow ($\phi \approx 85°$).

The green circle in panel (a) of Fig. 4 highlights the focusing between short nondispersive wave components with $k \approx 2$ and a few long, nondispersive, waves belonging to region **C** of the dispersion maps of Fig. 2. These long waves appear as white dots concentrated at the centerline where $x/t \approx 0.7$. Together with the highly focused short waves of the wave packet front, these long modes may play a role in the generation of the intense and long-lasting shear layer that connects the front of the wave packet to its core, the so-called "permanent scar" observed by Landhal.[50,51] Other focusing loci are indicated with yellow circles in the same panel [see Fig. 4(a)].

The asymptotic spreading rates can be directly inferred from the propagation scheme shown in Figs. 4(a) and 4(b). The lines that connect the origin to the point of maximum spreading (white line) for the entire packet and (red line) for the inner rhomboid-shaped region can be observed. These lines define the spreading half-angle ψ_{spread}. Figure 6 shows the Reynolds number effect on the asymptotic shape of wave packets, such as that presented in Figs. 4(a) and 4(b). As $\mathcal{R}$ increases, an increment of the spreading angle ψ_{spread} is found to be related to the concomitant narrowing and slowing of the wave packet core as $\mathcal{R}$ increases, which results in an elongation of the arrow-shaped structure. Calculated values of ψ_{spread} agree well with laboratory observations, as evidenced by the comparison with Fig. 4(d). Streamwise spreading in the simulation is computed by searching for the portion of domain that contains 95% of the energy. The boundaries of this region are named x_{rear} and x_{front}, respectively. In particular, for a generic quantity $\tilde{q}$, they are defined as the location of the 2.5th and 97.5th percentiles of the xy-reduced squared variable

$$x_{\mathrm{rear,front}}(t): \int_{-\infty}^{x_{0\%}} \langle \tilde{q}^2 \rangle_z \mathrm{d}x = C \int_{-\infty}^{\infty} \langle \tilde{q}^2 \rangle_z \mathrm{d}x, \quad (24)$$

where $\langle \tilde{q} \rangle_z (t, x, y) = L_z^{-1} \int \tilde{q} \mathrm{d}z$ (L_z is the domain size in the spanwise direction), $C = 0.25$ and 0.975 for the rear and front, respectively. Analogous metrics are defined in detail in Appendix, and a detailed review of these specific spatial features corresponding to our simulations [see Fig. 4(c)] is reported in Table I and in Fig. 9 of Appendix. A review of literature experiments is given in Table II. Here, the values are either explicitly stated by the authors or extracted from visualizations. Most of them refer to turbulent/laminar interfaces. It can be observed that the rear of the inner

to investigate the time dependence of ρ_w. This requires the computation of time-dependent dispersion relations in the framework of the nonmodal stability analysis. This task is delicate because in the early transient the phase speeds may experience rapid fluctuations,[25] and will be postponed to a future study. Interestingly, we observe a large wave concentration in the front and at the wingtips of the inner rhomboid-shaped region.

At the wingtips, the wave components are quite oblique with angles around $75°$. These waves are the most algebraically unstable, that is, they experience the largest growth in transient kinetic energy and enstrophy in the intermediate term. Moreover, as shown here,

FIG. 6. Asymptotic wave packet representation: Reynolds number effect. The propagation of the wavenumber magnitude (left) and the wave angle (right) are shown for $\mathcal{R} = [500, 1000, 2000, 4000]$ (top to bottom).

turbulent region corresponds to the center of our linear spots and that it moves at a speed nearly equal to one half of the centerline channel speed. The spot front moves faster, with a speed of about 0.7–$0.8U_C$ that is almost equal to the values found for x_{front} in the linear spots. The lateral spreading rates we observe compare well with the values obtained from experiments that lie in the range $(0.06, 0.12)$, while z_{spread} is somewhere between 0.06 and 0.12, depending on which field component is considered. If the kinetic energy or the enstrophy is considered for this computation, the spreading half-angle is about $10°$. This value is also close to that measured from the turbulent core of laboratory spots.

TABLE I. Spreading rates at $\mathcal{R} = 1000$ obtained as the time average for $t \in [15, 35]$. The spreading rates of the field components are computed at a fixed distance from the wall, $y = -0.6$, while the kinetic energy and the enstrophy are y-averaged.

	$\mathcal{R} = 1000$							
	$\tilde{u}$	$\tilde{v}$	$\tilde{w}$	$\langle E \rangle_y$	$\tilde{\omega}_x$	$\tilde{\omega}_y$	$\tilde{\omega}_z$	$\langle \Omega \rangle_y$
x_G	0.51	0.45	0.50	0.54	0.50	0.57	0.56	0.56
x_{rear}	0.31	0.24	0.38	0.33	0.38	0.42	0.39	0.35
x_{front}	0.74	0.65	0.79	0.80	0.82	0.73	0.79	0.82
z_{spread}	0.08	0.12	0.09	0.04	0.08	0.05	0.08	0.05
ψ_{spread}	$10.4°$	$17.4°$	$15.3°$	$10.1°$	$14.1°$	$8.50°$	$9.92°$	$10.3°$

V. CONCLUSIONS

We have shown the existence of linear dispersive wave focusing inside one of the archetypal Navier–Stokes incompressible shear flows, the plane Poiseuille flow (unstratified and in the absence of a background rotation). This was done by investigating the dispersion relation of least-damped, small-amplitude perturbation waves in this flow for a three-decade range of wavenumbers and a four-decade range of Reynolds numbers.

Looking at the dispersion map in the limit of least-damped waves, we have shown the existence of several sub-regions with remarkably variable levels of dispersion across the parameters space. This particular scenario yields dispersive focusing. We have deduced a propagation scheme based on the saddle point asymptotic approximation and by using the directional distribution of the numerically computed asymptotic group velocity. This model has proved to recover the morphology and propagation properties of wave packets under linearized dynamics. We also highlight that several of the propagation features shown here are also observed in laboratory experiments and in direct numerical simulations, where transition to turbulence can occur for Reynolds numbers above the global stability threshold, and laminar flow coexists with turbulent patches. In particular, the analysis suggests a correlation between the rhomboid-shaped region in our model, where focusing is high, and the region where strong nonlinear coupling is more likely to be triggered in the real system. In other dynamical contexts, in particular that of surface water waves, the propagation pairing between long and short waves and the mutual influence of their angle of

TABLE II. Spreading rates (normalized by the centerline velocity U_C) of localized perturbations and turbulent spots from literature experiments on PPF. These values mostly refer to the turbulent/laminar interface of developed self-sustaining spots. Here, the effect of the Reynolds number $\mathcal{R}$ on the wave packet's shape is shown in Fig. 6.

	$\mathcal{R}$	x_G	x_{rear}	x_{front}	z_{spread}	ψ_{turb}
C-1982[15]	1000	0.5	0.33	0.6	…	8°
A-1986[16]	1100–2200	…	0.62–0.52	0.75–0.8	…	6°–12°
HA-1987[52]	1200–3000	0.65	0.56	0.83	0.12	7°–15°
KA-1990[53]	1600	0.65	0.55	0.7–0.85	0.09–0.2	8°
HK-1991[23]	1500	0.64	0.55	0.70–0.8	0.08–0.12	8°–9°
K-1992[17]	1600	0.65–0.7	0.55	0.82	0.06	6°–8°
LAW-2013[18]	2000	0.66	0.54	0.84	…	…
LAW-2013[18]	3000	0.49	0.62	0.84	…	…

inclination have led the way to a new understanding into the analysis of both linear and nonlinear wave interactions.

This dynamical aspect has not been considered in great detail in the context of turbulence transition in shear flows. This likely occurred because wavenumbers with values close to the region of the stability map where unconditional instability takes place were predominantly investigated. In the sub-critical transitional context, fully developed turbulence and waves coexist, a scenario which goes beyond the so-called wave-turbulence. The dispersive focusing in the wave packet's early evolution, shown in this study, leads to the conjecture that this phenomenon may play an important role in promoting nonlinear wave interaction and in the consequent transition to turbulence, a conjecture that opens up a new investigation perspective for the context of nonlinear dispersive focusing of perturbation waves in shear flows.

APPENDIX: NUMERICAL SIMULATIONS

1. Methods for the initial-value problem

Numerical simulations [see Fig. 4(c)] have been performed via a MATLAB software, built to solve the three-dimensional, linearized, incompressible Navier–Stokes equations in planar channel flows. Initial perturbations of arbitrary shape can be specified. The periodic boundary conditions in the x and z directions allow us to use a Fourier spectral numerical method.

A pre-processing routine specifies the base flow and the simulation parameters (the Reynolds number $\mathcal{R}$, the domain size L_x and L_z, the time and space discretization, and the initial conditions in the physical space). In detail, we represent the solution for any perturbation variable $\tilde{q}$ of a general, 3D, small perturbation as

$$\tilde{q}(\boldsymbol{x}, t) = \text{Re}\left\{\frac{1}{(2\pi)^2}\int\int a_q(t, y; \alpha, \beta)e^{i\alpha x + i\beta z}\,\mathrm{d}\alpha\,\mathrm{d}\beta\right\}, \quad (A1)$$

where Re stands for the real part. It was convenient to separate variables and split a_q into two factors

$$a_q(t, y; \alpha, \beta) = \hat{q}(t, y; \alpha, \beta)\hat{f}(\alpha, \beta), \quad (A2)$$

where $\hat{q}$ is the complex-valued Fourier coefficient of an individual wave [that is, the solution of the Orr–Sommerfeld/Squire initial-value problem, Eqs. (7) and (8)]. The expression $\hat{f}(\alpha, \beta)$ gives the distribution in the x–z plane, where we have set a Gaussian distribution of thickness tuned by the parameter $\gamma = 0.1$ in order to simulate a localized 3D impulsive disturbance. Further details on the initial condition chosen for the simulation shown in the present study are reported below in Subsection 2 of Appendix. Numerically, the integral (A1) is discretized as

$$\tilde{q}(x, y, z, t) = \text{Re}\left\{\frac{1}{N_x N_z}\sum_{j=-\frac{N_x}{2}}^{\frac{N_x}{2}-1}\sum_{k=-\frac{N_z}{2}}^{\frac{N_z}{2}-1} a_q(t, y; \alpha, \beta)e^{i\alpha_j x + i\beta_k z}\right\}, \quad (A3)$$

where N_x and N_z are the number of grid points and $\alpha_j = \frac{2\pi j}{N_x \Delta x}$, $\beta_i = \frac{2\pi i}{N_z \Delta z}$ are the discrete streamwise and spanwise wavenumbers, respectively. The temporal evolution of the individual wave components is analytically described; therefore, the time grid can be arbitrary and has no effect on the accuracy of the computation. A fine grid is needed for post-processing purposes only, such as movie visualizations or the computation of spreading rates. A summary of the chosen simulation parameters for the linear spot of Fig. 4(c) is reported in Table III.

The processing core is dedicated to the computation of the temporal evolution of individual Fourier components. It is based on a semi-analytical solution of the Orr–Sommerfeld and Squire initial-value problem via the Galërkin method. Here, an eigenfunction expansion with Chandrasekhar–Reid functions[36] is used to represent the solution in the wall normal direction y. A major issue

TABLE III. Wave packet parameters for the simulation of Fig. 4(c) in the main text. $(x0, z_0)$ is the initial spot's location in x–z plane and γ is the standard deviation of the Gaussian function used as initial condition to simulate the localized 3D spot [see Eq. (A11) for further details]. $L_x \times L_y \times L_z$ is the dimensionless domain size, containing $N_x \times N_y \times N_z$ computational grid points. T_{max} is the dimensionless final time and Δt is the time step.

3D linear	
x_0	0
z_0	0
γ	0.1
$\mathcal{R}$	1000
L_x	120
L_y	2
L_z	60
N_x	256
N_y	129
N_z	128
T_{max}	120
Δt	0.3

related to the OS–Squire initial value problem is the intrinsic high sensitivity of the OS operator to numerical perturbations, specifically at large $\mathcal{R}$ and wavenumbers.[54] This may cause large inaccuracy in the computation of the eigenvalues at the intersection of the branches. Whilst the least-damped modes are much less affected by such sensitivity, it can significantly affect the numerical solution during the early/intermediate transient. In fact, it is intrinsically related to the nonorthogonal nature of the eigenvectors. We prevent this issue by using 300 modes in the expansion. The full description of the method can be found in the supplementary material of Ref. 25 and in Appendix A of Ref. 27. This method has also been used in our recent study on the wave enstrophy.[26] Source codes are available at https://areeweb.polito.it/ricerca/philofluid/software.html.

At a second stage, a dedicated routine performs the inverse Fourier transform (FT) in order to obtain the perturbation velocity

and vorticity fields in the physical space. Post-processing routines are used to compute the wave packet center and the spreading rates, and to produce movies.

2. Initial perturbation for a localized 3D spot

According to the representation (A2), the coefficients of the initial condition are

$$a_q^0(y; \alpha, \beta) = \hat{q}^0(y; \alpha, \beta)\hat{f}(\alpha, \beta). \tag{A4}$$

The velocity–vorticity formulation requires the initial wall-normal velocity $\tilde{v}^0(y)$ and the initial wall-normal vorticity $\tilde{\omega}_y^0(y)$. Thus, we specify

$$a_v^0(y; \alpha, \beta) = \hat{v}^0(y; \alpha, \beta)\hat{f}(\alpha, \beta), \tag{A5}$$

$$a_{\omega_y}^0(y; \alpha, \beta) = \hat{\omega}_y^0(y; \alpha, \beta)\hat{f}(\alpha, \beta). \tag{A6}$$

The coefficients of the initial streamwise and spanwise initial components of velocity read

$$a_u^0(y; \alpha, \beta) = \hat{u}^0(y; \alpha, \beta)\hat{f}(\alpha, \beta), \tag{A7}$$

$$a_w^0(y; \alpha, \beta) = \hat{w}^0(y; \alpha, \beta)\hat{f}(\alpha, \beta), \tag{A8}$$

and, due to the incompressibility condition and the definition of the velocity curl, they can be derived *a posteriori* as follows:

$$\hat{u}^0(y; \alpha, \beta) = \frac{i}{k^2}\left[\alpha\partial_y\hat{v}^0(y) - \beta\hat{\omega}_y^0(y)\right], \tag{A9}$$

$$a_w^0(y) = \frac{i}{k^2}\left[\beta\partial_y\hat{v}^0(y) + \alpha\hat{\omega}_y^0(y)\right].. \tag{A10}$$

The cross-shear velocity $\hat{v}^0(y)$ was chosen in order to guarantee a transient growth of the perturbation kinetic energy for any wavenumber included in the packet ($\hat{v}^0(y)$ is shown in Fig. 7). The corresponding
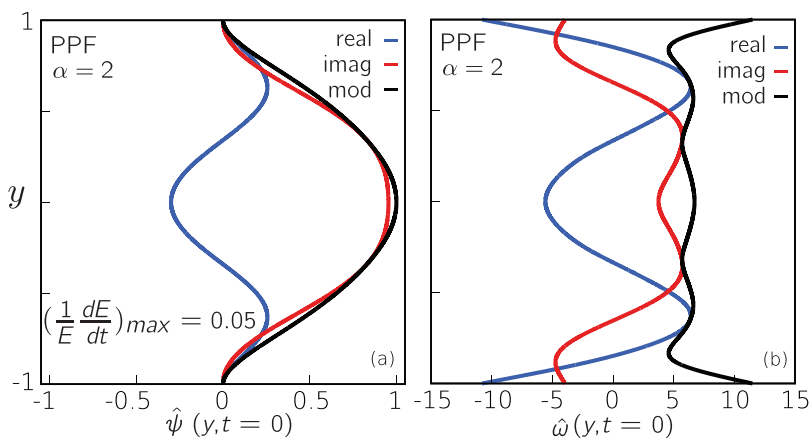
FIG. 7. Initial optimal condition, y-distribution. This figure is part of Fig. 8 in Ref. 26, and it is reported here for the reader's convenience. The optimization procedure seeks the smooth perturbation which maximizes the kinetic energy growth rate $E^{-1}(dE/dt)$ at fixed values of k and $\mathcal{R}$, while exciting both symmetric and antisymmetric Orr–Sommerfeld modes. Zero initial wall-normal vorticity is set.
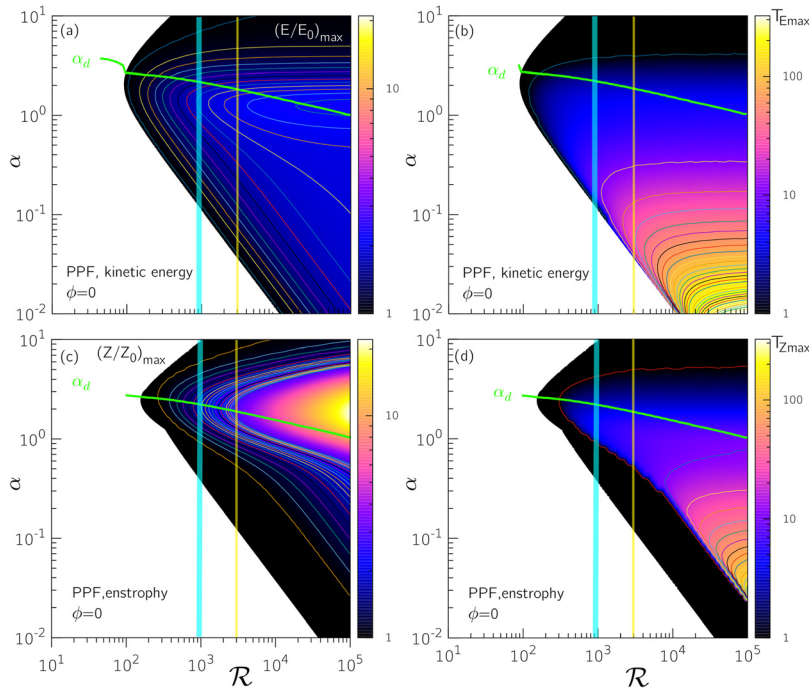
FIG. 8. Maximal kinetic energy and enstrophy achieved during the transient and related time scales for longitudinal perturbation waves ($\phi = 0$) in PPF given by the initial condition of Fig. 7. Panels (a) and (c) show the wavenumber-Reynolds number map of maximal transient growth reached during the transient in terms of normalized kinetic energy (E/E_0) and enstrophy (Z/Z_0), respectively. The time instant corresponding to the maximum energy/enstrophy is shown in the right panels. Each map is built from 3600 numerical simulations of the Orr–Sommerfeld/Squire initial-value problem. The light blue vertical bands represent the global stability threshold, $\mathcal{R}_g$: values collected from experiments in the literature are around 840.[37] In two dimensions, nonlinear analysis of PPF leads to a transitional value of about 2900 (vertical yellow line).[55] The green curve represents the dispersive-to-nondispersive transition between subregions **A** and **B** in this study. Reproduced with permission from Figs. 5(b) and 5(d) and Fig. SM 1 in Phys. Ref. E. **97**, 063102 (2018).[26] Copyright 2018 American Physical Society.

maximal growth for longitudinal waves is shown in Fig. 8. The evolution of this initial condition for individual waves and 2D wave packets was previously investigated in Ref. 26. This initial velocity profile was obtained from an optimization procedure that seeks the perturbation that maximizes the kinetic energy growth rate $E^{-1}(dE/dt)$, at fixed values of k and $\mathcal{R}$. A similar optimization procedure has recently been adopted in the nonmodal stability analysis of time-dependent jet flows by Nastro et al.[47] Such an initial condition excites both symmetric and anti-symmetric Orr–Sommerfeld modes; it is smooth and has a relatively simple shape. Zero initial wall-normal vorticity is set. The resulting initial velocity field is a quadrupole of counter-rotating vortices. As discussed before, a Gaussian distribution was chosen for $f(x, z)$. This was done in order to represent a smooth, spatially localized perturbation ($\gamma = 0.1$, that is one tenth of the half thickness of the channel) having a similar distribution to disturbances usually introduced in laboratory experiments (where dye is typically injected from a small hole in the wall[15,17,53]) or numerical experiments:[56]

$$f(x, z) = \frac{1}{\gamma\sqrt{2\pi}} e^{-\left[(x-x_0)^2 + (z-z_0)^2\right]/2\gamma^2}, \quad \text{(A11)}$$

$$\hat{f}(\alpha, \beta) = \mathcal{F}\{f(x, z)\}, \quad \text{(A12)}$$

where $\mathcal{F}$ denotes the Fourier transform (FT). The online movie movie_PPF_R_1000_V.avi (Multimedia view) shows the evolution of the wall-normal perturbation velocity $v(x, y = 0.6, z)$ for the linear spot shown in Fig. 4(c) ($\mathcal{R} = 1000$, with simulation parameters as reported in Table III). The movie movie_waterfall_PPF_Re1000_V.avi (Multimedia view) shows a pseudo-3D visualization of the wall-normal perturbation velocity for the same simulation.

3. Wave packet spatial spreading rates

The wave packet energy centroid is computed for each squared field component (at a fixed distance from the wall $y_0 = -0.6$) and for the y-averaged kinetic energy and enstrophy. We use the following notations for the averaging operations over y, z, and x (that is, for xz-, xy-, and yz-reduced quantities, respectively)
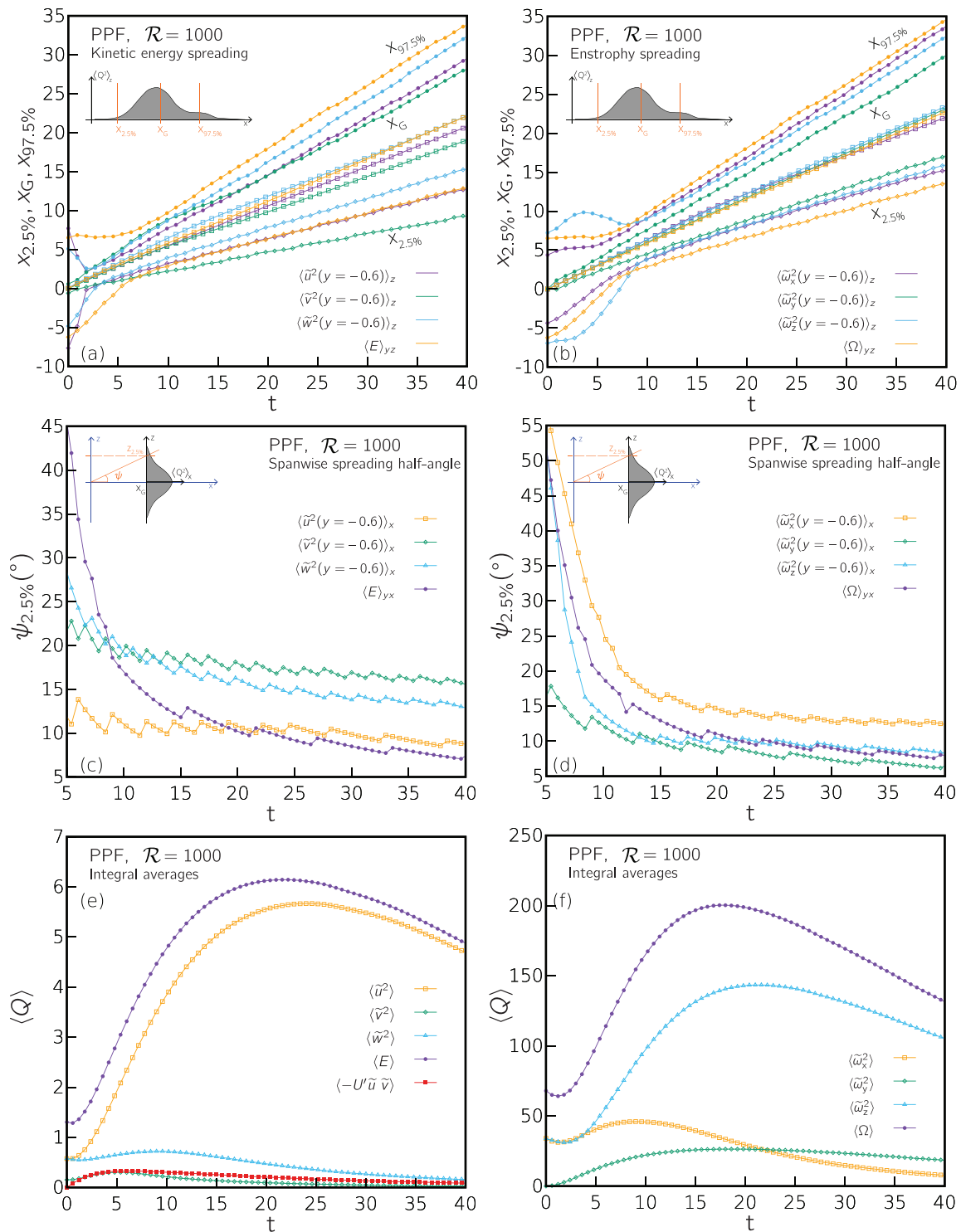
$$\langle\tilde{q}\rangle_y(t, x, z) = \frac{1}{L_y}\int \tilde{q}\,dy,$$

$$\langle\tilde{q}\rangle_z(t, x, y) = \frac{1}{L_z}\int \tilde{q}\,dz, \quad \text{(A13)}$$

$$\langle\tilde{q}\rangle_x(t, y, z) = \frac{1}{L_x}\int \tilde{q}\,dx.$$

The wave packet center of a generic field component $\tilde{q}$ is then defined as

$$x_G(t, y_0) = \frac{\int x\langle\tilde{q}^2\rangle_z\,dx}{\int \langle\tilde{q}^2\rangle_z\,dx}. \quad \text{(A14)}$$

In particular, it can be defined with respect to the average kinetic energy $\langle E\rangle_y = \langle\tilde{u}^2 + \tilde{v}^2 + \tilde{w}^2\rangle_y$ and enstrophy $\langle\Omega\rangle_y = \langle\tilde{\omega}_x^2 + \tilde{\omega}_y^2 + \tilde{\omega}_z^2\rangle_y$

$$x_G(t) = \frac{\int \langle\langle E\rangle_y\rangle_z x\,dx}{\int \langle\langle E\rangle_y\rangle_z\,dx}, \quad x_G(t) = \frac{\int \langle\langle\Omega\rangle_y\rangle_z x\,dx}{\int \langle\langle\Omega\rangle_y\rangle_z\,dx}. \quad \text{(A15)}$$

FIG. 9. Spreading rates [panels (a) and (b)], spreading half-angles [panels (c) and (d)], and volume-averaged energy and enstrophy [panels (e) and (f)] for the numerical simulation of Fig. 4(c) [see definitions (A15)–(A19) in Subsection 3 of the Appendix]. Reproduced with permission from Fig. 28 in F. Fraternale, "Internal waves in fluid flows: Possible coexistence with turbulence," Ph.D. thesis (Politecnico di Torino, Torino, Italy, 2017).[27] Copyright 2017 Author, licensed under a Creative Commons Attribution (CC BY) License.

TABLE IV. Spreading rates at $\mathcal{R} = 500$, time averages computed for $t \in [15, 35]$. The spreading rates of the field components are computed at a fixed distance from the wall, $y = -0.6$, while the kinetic energy and the enstrophy are y-averaged.

	$\tilde{u}$	$\tilde{v}$	$\tilde{w}$	$\langle E \rangle_y$	$\tilde{\omega}_x$	$\tilde{\omega}_y$	$\tilde{\omega}_z$	$\langle \Omega \rangle_y$
				$\mathcal{R} = 500$				
x_G	0.54	0.50	0.56	0.56	0.54	0.59	0.59	0.58
x_{rear}	0.33	0.27	0.41	0.36	0.42	0.43	0.43	0.38
x_{front}	0.75	0.71	0.84	0.80	0.84	0.78	0.81	0.80
z_{spread}	0.08	0.12	0.10	0.06	0.08	0.06	0.08	0.05
ψ_{spread}	10.5°	16.1°	15.1°	10.2°	13.8°	9.43°	9.98°	10.2°

The streamwise spreading is computed by seeking the portion of the domain which contains 95% of the energy. The boundaries of this region are named x_{rear} and x_{front}, respectively. They are defined as the locations of the 2.5th and 97.5th percentile of the xy-reduced, squared variable being considered, respectively,

$$x_{rear}(t) : \int_{-\infty}^{x_{2.5}\%} \langle \tilde{q}^2 \rangle_z dx = 0.025 \int_{-\infty}^{\infty} \langle \tilde{q}^2 \rangle_z dx, \quad (A16)$$

$$x_{front}(t) : \int_{-\infty}^{x_{97.5}\%} \langle \tilde{q}^2 \rangle_z dx = 0.975 \int_{-\infty}^{\infty} \langle \tilde{q}^2 \rangle_z dx. \quad (A17)$$

Analogously, the spanwise spreading and the spreading half-angle are computed from the xz-reduced squared quantities

$$z_{spread}(t) : \int_{-\infty}^{z_{2.5}\%} \langle \tilde{q}^2 \rangle_x dz = 0.025 \int_{-\infty}^{\infty} \langle \tilde{q}^2 \rangle_x dz, \quad (A18)$$

$$\psi_{spread} = \tan^{-1}\left(\frac{z_{spread}}{x_G}\right). \quad (A19)$$

Figure 9 presents the spreading rates of a wave packet at $\mathcal{R} = 1000$. Furthermore, Table IV displays the spreading rate data for the $\mathcal{R} = 500$ case.

DATA AVAILABILITY

The data that support the findings of this study are available from the corresponding author upon reasonable request.

REFERENCES

[1]G. B. Whitham, *Linear and Nonlinear Waves* (John Wiley & Sons, New York, 1974).

[2]C. Sulem and P. L. Sulem, *The Nonlinear Schrödinger Equation* (Springer Science & Business Media, 1991).

[3]A. D. D. Craik, *Wave Interactions and Fluid Flows* (Cambridge University Press, 1985).

[4]V. I. Karpman and D. Haar, *Non-Linear Waves in Dispersive Media: International Series of Monographs in Natural Philosophy* (Elsevier, 2026).

[5]M. J. Ablowitz and H. Segur, "On the evolution of packets of water waves," J. Fluid Mech. **92**, 691–715 (1979).

[6]K. B. Dysthe and K. Trulsen, "Note on breather type solutions of the NLS as models for freak-waves," Phys. Scr. **T82**, 48–52.

[7]K. L. Henderson, D. H. Peregrine, and J. W. Dold, "Unsteady water wave modulations: Fully nonlinear solutions and comparison with the nonlinear Schrödinger equation," Wave Motion **29**, 341–361 (1999).

[8]M. Onorato, A. R. Osborne, M. Serio, and S. Bertone, "Freak waves in random oceanic sea states," Phys. Rev. Lett. **86**, 5831 (2001).

[9]A. Slunyaev, C. Kharif, E. Pelinovsky, and T. Talipova, "Nonlinear wave focusing on water of finite depth," Physica D **173**, 77–96 (2002).

[10]M. K. Smit, "New focusing and dispersive planar component based on an optical phased array," Electron. Lett. **24**, 385–386 (1988).

[11]M. V. Morkovin, "On the many faces of transition," in *Viscous Drag Reduction* edited by S. Wells (Springer Nature, 1969), pp. 1–31.

[12]L. N. Trefethen, A. E. Trefethen, S. C. Reddy, and T. A. Driscoll, "Hydrodynamic stability without eigenvalues," Science **261**, 578–584 (1993).

[13]P. J. Schmid, "Nonmodal stability theory," Annu. Rev. Fluid Mech. **39**, 129–162 (2007).

[14]H. W. Emmons, "The laminar-turbulent transition in a boundary layer: Part I," J. Aeronaut. Sci. **18**, 490–498 (1951).

[15]D. R. Carlson, S. E. Widnall, and M. Peeters, "A flow-visualization study of transition in plane Poiseuille flow," J. Fluid Mech. **121**, 487–505 (1982).

[16]F. Alavyoon, D. S. Henningson, and P. H. Alfredsson, "Turbulent spots in plane Poiseuille flow–flow visualization," Phys. Fluids **29**, 1328–1331 (1986).

[17]B. G. B. Klingmann, "On transition due to three-dimensional disturbances in plane Poiseuille flow," J. Fluid Mech. **240**, 167–195 (1992).

[18]G. Lemoult, J. L. Aider, and J. E. Wesfreid, "Turbulent spots in a channel: Large-scale flow and self-sustainability," J. Fluid Mech. **731**, R1 (2013).

[19]G. Lemoult, K. Gumowski, J.-L. Aider, and J. E. Wesfreid, "Turbulent spots in channel flow: An experimental study," Eur. Phys. J. E **37**, 1–11 (2014).

[20]L. Klotz, G. Lemoult, I. Frontczak, L. S. Tuckerman, and J. E. Wesfreid, "Couette-Poiseuille flow experiment with zero mean advection velocity: Subcritical transition to turbulence," Phys. Rev. Fluids **2**, 043904 (2017).

[21]L. Klotz and J. E. Wesfreid, "Experiments on transient growth of turbulent spots," J. Fluid Mech. **829**, R4 (2017).

[22]A. Lundbladh and A. V. Johansson, "Direct simulation of turbulent spot in plane Couette flow," J. Fluid Mech. **229**, 499–516 (1991).

[23]D. S. Henningson and J. Kim, "On turbulent spots in plane Poiseuille flow," J. Fluid Mech. **228**, 183–205 (1991).

[24]Y. Duguet, P. Schlatter, D. S. Henningson, and B. Eckhardt, "Self-sustained localized structures in a boundary-layer flow," Phys. Rev. Lett. **108**, 044501 (2012).

[25]F. De Santi, F. Fraternale, and D. Tordella, "Dispersive-to-nondispersive transition and phase-velocity transient for linear waves in plane wake and channel flows," Phys. Rev. E **93**, 033116 (2016).

[26]F. Fraternale, L. Domenicale, G. Staffilani, and D. Tordella, "Internal waves in sheared flows: Lower bound of the vorticity growth and propagation discontinuities in the parameter space," Phys. Rev. E **97**, 063102 (2018).

[27]F. Fraternale, "Internal waves in fluid flows: Possible coexistence with turbulence," Ph.D. thesis (Politecnico di Torino, Torino, Italy, 2017).

[28]W. M'F. Orr, "The stability or instability of the steady motions of a perfect liquid and a viscous liquid. Part I," Proc. R. Ir. Acad. **27**, 9–68 (1907). https://www.jstor.org/stable/20490590

[29]H. B. Squire and R. V. Southwell, "On the stability for three-dimensional disturbances of viscous fluid flow between parallel walls," Proc. R. Soc. London, Ser. A **142**, 621–628 (1933).

[30]L. Muschietti and C. T. Dum, "Real group velocity in a medium with dissipation," Phys. Plasmas **5**, 1383–1397 (1993).

[31]E. Sonnenschein, I. Rutkevich, and D. Censor, "Wave packets, rays, and the role of real group velocity in absorbing media," Phys. Rev. E **57**, 1005 (1998).

[32]V. Gerasik and M. Stastna, "Complex group velocity and energy transport in absorbing media," Phys. Rev. E **81**, 056602 (2010).

[33]M. Gaster, "On the generation of spatially growing waves in a boundary layer," J. Fluid Mech. **22**, 433–441 (1965).

[34]A. D. D. Craik, "On the development of singularities in linear dispersive systems," J. Fluid Mech. **538**, 137–151 (2005).

[35]W. O. Criminale, T. L. Jackson, and R. D. Joslin, *Theory and Computation in Hydrodynamic Stability* (Cambridge University Press, 2019).

[36]S. Chandrasekhar, *Hydrodynamic and Hydromagnetic Stability* (Oxford University Press, 1961).

[37]P. Manneville, "Transition to turbulence in wall-bounded flows: Where do we stand?," Mech. Eng. Rev. **3**, 1–23 (2016).

[38]S. A. Orszag, "Accurate solution of the Orr–Sommerfeld stability equation," J. Fluid Mech. **50**, 689–703 (1971).

[39]L. M. Mack, "A numerical study of the temporal eigenvalue spectrum of the Blasius boundary layer," J. Fluid Mech. **73**, 497–520 (1976).

[40]J. J. Duistermaat, "Oscillatory integrals, Lagrange immersions and unfolding of singularities," Commun. Pure Appl. Math. **27**, 207–281 (1974).

[41]C. M. Bender and S. A. Orszag, *Advanced Mathematical Methods for Scientists and Engineers I: Asymptotic Methods and Perturbation Theory*, Advanced Mathematical Methods for Scientists and Engineers (Springer, 1978).

[42]T. B. Benjamin, "The development of three-dimensional disturbances in an unstable film of liquid flowing down an inclined plane," J. Fluid Mech. **10**, 401–419 (1961).

[43]W. O. Criminale and L. S. G. Kovasznay, "The growth of localized disturbances in a laminar boundary layer," J. Fluid Mech. **14**, 59–80 (1962).

[44]A. D. D. Craik, "The development of wavepackets in unstable flows," Proc. R. Soc. London, Ser. A **373**, 457–476 (1981).

[45]C. Petz, H.-C. Hege, K. Oberleithner, M. Sieber, C. N. Nayeri, C. O. Paschereit, I. Wygnanski, and B. R. Noack, "Global modes in a swirling jet undergoing vortex breakdown," Phys. Fluids **23**, 091102 (2011).

[46]D. A. Bistrian, "Parabolized Navier-Stokes model for study the interaction between roughness structures and concentrated vortices," Phys. Fluids **25**, 104103 (2013).

[47]G. Nastro, J. Fontane, and L. Joly, "Optimal perturbations in viscous round jets subject to Kelvin–Helmholtz instability," J. Fluid Mech. **900**, A13 (2020).

[48]G. I. Barenblatt, *Scaling, Self-Similarity and Intermediate Asymptotics*, Cambridge Texts in Applied Mathematics (Cambridge University Press, 1996).

[49]Y. Duguet, A. P. Willis, and R. R. Kerswell, "Slug genesis in cylindrical pipe flow," J. Fluid Mech. **663**, 180–208 (2010).

[50]M. T. Landahl, "Wave breakdown and turbulence," SIAM J. Appl. Math. **28**, 735–756 (1975).

[51]M. T. Landahl, "A note on an algebraic instability of inviscid parallel shear flows," J. Fluid Mech. **98**, 243–251 (1980).

[52]D. S. Henningson and P. H. Alfredsson, "The wave structure of turbulent spots in plane Poiseuille flow," J. Fluid Mech. **178**, 405–421 (1987).

[53]B. G. B. Klingmann and P. H. Alfredsson, "Turbulent spots in plane Poiseuille flow: Measurement of the velocity-field," Phys. Fluids A **2**, 2183–2195 (1990).

[54]S. C. Reddy, P. J. Schmid, and D. S. Henningson, "Pseudospectra of the Orr–Sommerfeld operator," SIAM J. Appl. Math. **53**, 15–47 (1993).

[55]B. J. Bayly, S. A. Orszag, and T. Herbert, "Instability mechanisms in shear-flow transition," Annu. Rev. Fluid Mech. **20**, 359–391 (1988).

[56]D. S. Henningson, A. Lundbladh, and A. V. Johansson, "A mechanism for bypass transition from localized disturbances in wall-bounded shear flows," J. Fluid Mech. **250**, 169–207 (1993).